



**HAL**  
open science

## **Biosynthesis of magnetic nanoparticles from nano-degradation products revealed in human stem cells**

Aurore van de Walle, Anouchka Plan Sangnier, Ali Abou-Hassan, Alberto Curcio, Miryana Hemadi, Nicolas Menguy, Yoann Lalatonne, Nathalie Luciani, Claire Wilhelm

### ► **To cite this version:**

Aurore van de Walle, Anouchka Plan Sangnier, Ali Abou-Hassan, Alberto Curcio, Miryana Hemadi, et al.. Biosynthesis of magnetic nanoparticles from nano-degradation products revealed in human stem cells. *Proceedings of the National Academy of Sciences of the United States of America*, 2019, 116 (10), pp.4044-4053. 10.1073/pnas.1816792116 . hal-02409281

**HAL Id: hal-02409281**

**<https://hal.science/hal-02409281>**

Submitted on 13 Dec 2019

**HAL** is a multi-disciplinary open access archive for the deposit and dissemination of scientific research documents, whether they are published or not. The documents may come from teaching and research institutions in France or abroad, or from public or private research centers.

L'archive ouverte pluridisciplinaire **HAL**, est destinée au dépôt et à la diffusion de documents scientifiques de niveau recherche, publiés ou non, émanant des établissements d'enseignement et de recherche français ou étrangers, des laboratoires publics ou privés.



# Biosynthesis of magnetic nanoparticles from nano-degradation products revealed in human stem cells

Aurore Van de Walle<sup>a</sup>, Anouchka Plan Sangnier<sup>a,b</sup>, Ali Abou-Hassan<sup>c</sup>, Alberto Curcio<sup>a</sup>, Miryana Hémadi<sup>d</sup>, Nicolas Menguy<sup>e</sup>, Yoann Lalatonne<sup>b,f</sup>, Nathalie Luciani<sup>g</sup>, and Claire Wilhelm<sup>a,1</sup>

<sup>a</sup>Laboratoire Matière et Systèmes Complexes, UMR 7057, CNRS and University Paris Diderot, 75205 Paris Cedex 13, France; <sup>b</sup>INSERM, U1148, Laboratory for Vascular Translational Science, Université Paris 13, Sorbonne Paris Cité, F-93017 Bobigny, France; <sup>c</sup>Sorbonne Université, CNRS, Physico-chimie des Electrolytes et Nanosystèmes Interfaciaux, F-75005 Paris, France; <sup>d</sup>Interfaces, Traitements, Organisation et Dynamique des Systèmes, Université Paris Diderot, Sorbonne Paris Cité, CNRS-UMR 7086, 75205 Paris Cedex 13, France; <sup>e</sup>Sorbonne Université, UMR CNRS 7590, Muséum National d'Histoire Naturelle, Institut de Recherche pour le Développement, Institut de Minéralogie, de Physique des Matériaux et de Cosmochimie, 75005 Paris, France; and <sup>f</sup>Services de Biochimie et de Médecine Nucléaire, Hôpital Avicenne Assistance Publique-Hôpitaux de Paris, F-93009 Bobigny, France

Edited by Catherine J. Murphy, University of Illinois at Urbana-Champaign, Urbana, IL, and approved January 17, 2019 (received for review October 1, 2018)

**While magnetic nanoparticles offer exciting possibilities for stem cell imaging or tissue bioengineering, their long-term intracellular fate remains to be fully documented. Besides, it appears that magnetic nanoparticles can occur naturally in human cells, but their origin and potentially endogenous synthesis still need further understanding. In an effort to explore the life cycle of magnetic nanoparticles, we investigated their transformations upon internalization in mesenchymal stem cells and as a function of the cells' differentiation status (undifferentiated, or undergoing adipogenesis, osteogenesis, and chondrogenesis). Using magnetism as a fingerprint of the transformation process, we evidenced an important degradation of the nanoparticles during chondrogenesis. For the other pathways, stem cells were remarkably "remagnetized" after degradation of nanoparticles. This remagnetization phenomenon is the direct demonstration of a possible neosynthesis of magnetic nanoparticles *in cellulo* and could lay some foundation to understand the presence of magnetic crystals in human cells. The neosynthesis was shown to take place within the endosomes and to involve the H-subunit of ferritin. Moreover, it appeared to be the key process to avoid long-term cytotoxicity (impact on differentiation) related to high doses of magnetic nanoparticles within stem cells.**

magnetic nanoparticles | biodegradation | biomineralization | stem cells | nano-bio interfaces

**M**agnetic nanoparticles (composed of iron oxides) have been observed in a variety of organisms. They are, for example, produced by the magnetic bacteria and used as a tool for their orientation along the geomagnetic field (1, 2). In humans, they have also been evidenced inside different types of cells; however, their exact role as well as the reason behind their occurrence are not fully understood (3).

In parallel, in nanomedicine, nanoparticles have attracted increased attention for their original properties that open up new possibilities for a wide range of treatments. Among them, magnetic nanoparticles have become a gold standard due to their composition—an iron-based core—that can be assimilated by the unique intrinsic iron metabolism of the organism. For this reason, they have already been approved for clinical use as contrast agent for magnetic resonance imaging (MRI) (4) and as iron supplement for the treatment of iron deficiency anemia, application restricted to patients with chronic kidney disease in a first instance, and recently expanded to all patients suffering from anemia (5). Upon these initial clinical successes, the field of research remains highly active, and a broader range of applications are currently assessed that go from thermal therapy to magnetic targeting (6–12).

The safety and efficacy of iron oxide nanoparticles, however, depend on their incorporation in the organism. Despite the fact that an exponential increase in the number of preclinical studies using magnetic nanoparticles for stem cell-based therapies have

been seen in the past two decades (13–16), their long-term intracellular fate remains virtually unexplored. In particular, the release of reactive iron species upon degradation and transformation of the nanoparticles stored in endosomes, at the very heart of stem cells, might be a source of cytotoxicity. Indeed, in vivo assimilation of magnetic nanoparticles relies on the transformation of the iron oxide core into soluble iron that can then be assimilated by various endogenous proteins implicated in iron oxidation, storage, and transport (17, 18). Studies performed in vivo have shown that i.v. administered nanoparticles are first internalized, mostly in liver and spleen, and then progressively degraded within months following injection (17, 19–22). Soluble iron then integrates the natural metabolism as shown by radioactive labeling of magnetic nanoparticles (<sup>59</sup>Fe) that evidenced labeled iron in the hemoglobin of newly formed erythrocytes 1 wk after injection (17) and intracellular storage in the core of the iron storage protein ferritin (21, 23, 24). Additionally, both in vivo and in vitro studies suggest that nanoparticles are degraded in the endosomes of cells via a wide variety of hydrolytic enzymes such as the lysosomal cathepsin L (25). Despite comprehensive assessment, these studies are only qualitative and reliable quantification of nanoparticles' transformations is still missing because of the complexity of the organism and the lack of specific

## Significance

**Naturally occurring magnetic nanoparticles have been detected in human cells; however, their origin and role remain unknown. In the present paper, the observation of long-term transformations of man-made magnetic nanoparticles internalized in human stem cells displays a mechanism regarding their assimilation. Indeed, the nanoparticles are first degraded by the stem cells, and then new magnetic nanoparticles are synthesized in situ from the released iron. This "remagnetization" phenomenon is observed under specific pathways only, involves the ferritin protein, and seems linked to a detoxification mechanism in case of iron excess. It also brings a direct experimental proof that magnetic nanoparticles can be synthesized by human cells.**

Author contributions: A.V.d.W., N.L., and C.W. designed research; A.V.d.W., A.P.S., A.A.-H., A.C., M.H., N.M., Y.L., N.L., and C.W. performed research; A.V.d.W., A.P.S., A.A.-H., and M.H. contributed new reagents/analytic tools; A.V.d.W., A.P.S., A.C., Y.L., and C.W. analyzed data; and A.V.d.W. and C.W. wrote the paper.

The authors declare no conflict of interest.

This article is a PNAS Direct Submission.

Published under the PNAS license.

<sup>1</sup>To whom correspondence should be addressed. Email: [claire.wilhelm@univ-paris-diderot.fr](mailto:claire.wilhelm@univ-paris-diderot.fr).

This article contains supporting information online at [www.pnas.org/lookup/suppl/doi:10.1073/pnas.1816792116/-DCSupplemental](http://www.pnas.org/lookup/suppl/doi:10.1073/pnas.1816792116/-DCSupplemental).

Published online February 13, 2019.

methodologies. Rare studies performed *in cellulo* have shown that nanoparticles' properties (e.g., coating, size) influence their transformations (26–28). However, the cellular factors that influence the lysosomal degradation still need to be explored.

Mesenchymal stem cells (MSCs) are a rich and clinically relevant cellular model. They are ideal to study the influence of cellular factors on magnetic nanoparticles' degradation due to their high variability potential as well as their therapeutic actuality. Indeed, iron oxide nanoparticles are being developed for regenerative medicine applications (i.e., to retain magnetically labeled MSCs at implantation site or to engineer organized tissues) (14, 29–34); their impact on stem cells is thus a necessary prerequisite. Studies assessing stem cell differentiation upon iron oxide nanoparticles' internalization have shown that high doses of nanoparticles can impact specific differentiation pathways, with chondrogenesis being more impacted than adipogenesis and osteogenesis (35–37). An explanation to this phenomenon might be that the assimilation of magnetic nanoparticles *in cellulo* varies depending on the differentiation pathway. It thus becomes an unmet need to correlate the differentiation status of stem cells (undifferentiated or undergoing chondrogenesis, adipogenesis, or osteogenesis) to magnetic nanoparticles' intracellular biotransformations.

The other asset of these nanoparticles is their magnetic imprint. Besides being the source of contrast for MRI, it also provides remote cellular forces for tissue stimulation and regenerative medicine (14, 38). Interestingly, their magnetic imprint can be used as the signature of the superparamagnetic iron oxide crystal, and thus of the nanoscopic integrity of the nanoparticles (39–42). Herein, magnetic biotransformations were first assessed by magnetometry, *in situ*, in real time, at the tissular scale, and reflecting the nanometric status. First, this magnetic follow-up demonstrated clear differences in the processing of nanoparticles by the cells depending on the differentiation pathway. Unexpectedly, undifferentiated stem cells as well as stem cells under adipogenesis and osteogenesis underwent a remagnetization phenomenon: They first lost 30–70% of their initial magnetization provided by the internalized nanoparticles during the first 3 d after internalization, but could then regain (almost totally) magnetization in the next days, without any new exposure to nanoparticles. This surprising remagnetization can only be explained by the neosynthesis of superparamagnetic iron oxide *in situ* upon initial degradation. Besides, such neosynthesis was found to be dependent on the expression of genes involved in iron metabolism. It also appeared to be modulated by proliferation level, culture conformation (2D vs. 3D), and specific differentiation pathway.

## Results

**Nanoparticles Processing by Stem Cells Monitored by Magnetism.** All applications involving magnetically labeled stem cells for imaging or manipulation start with the internalization of nanoparticles. Herein, cells were incubated with magnetic nanoparticles diluted in the extracellular medium, for a short time (30 min), and at different iron concentrations (0.05–0.4 mM). Whatever the dose, nanoparticles were internalized and localized into endosomes, as exemplified in the typical transmission electron microscopy (TEM) images of Fig. 1 *A–C* (other images are shown in *SI Appendix, Fig. S1*). For each concentration, the global magnetic moment (at field saturation) of cellular samples (systematically 200,000 cells) was measured by magnetometry (in EMUs). First, Fig. 1*D* shows the magnetization curve of the initial nanoparticles dispersed in water (10  $\mu$ L at  $[\text{Fe}] = 8$  mM). Fig. 1*E* then shows typical magnetization curves for the 200,000 cells incubated with increasing nanoparticle doses (0.2 and 0.4 mM). Magnetization curves were fitted using Langevin formalism (plain lines in graphs of Fig. 1 *D* and *E*) to retrieve the size distribution. For nanoparticles dispersed in water, the average magnetic diameter obtained by Langevin was found at

$8.4 \pm 0.3$  nm, with a polydispersity of  $0.31 \pm 0.02$ . The exact same magnetic diameter distribution was retrieved within the cells (average magnetic diameter,  $8.3 \pm 0.3$  nm; polydispersity,  $0.27 \pm 0.03$ ), demonstrating that the nanoparticles can be considered as magnetically noninteracting within the intracellular environment. This is explained by their superparamagnetic behavior and low magnetic anisotropy, resulting in Néel-like and not Brown-like relaxation (43). As magnetization dynamics can also be affected by the biological environment, such as the possible formation of a protein corona (44), the mass saturation magnetization was measured in cellular samples upon nanoparticles internalization, reaching an average value of  $64.2 \pm 2.6$  emu per g of iron, similar to that of the initial nanoparticles ( $65$  emu $\cdot$ g $^{-1}$ ). Moreover, identical magnetic susceptibility was retrieved for nanoparticles dispersed in water and internalized within cells (as demonstrated by the same Langevin fit), confirming that no effects from a potential opsonization of the nanoparticles could affect here the cellular magnetization measurements. Direct size analysis was also performed on TEM images (Fig. 1 *A–C* and *SI Appendix, Fig. S1*) and gave a similar average diameter for the nanoparticles, of  $8.4 \pm 0.2$  nm, and a polydispersity of 0.22. Both size distributions are superposed in Fig. 1*F*, with good correlation. Note, however, the large distribution, with nanoparticles size varying from 5 to 14 nm, typical for nanoparticles obtained by iron salts coprecipitation. Finally, the magnetization can be converted into a number of 8.4 nm magnetic nanoparticles per cell (see *Methods* for conversion), showing a resulting number that increases from about 10 million nanoparticles per cell (equivalent to 10 pg of cellular iron) to 20 million (20 pg) with incubated dose increasing from 0.2 to 0.4 mM. *SI Appendix, Fig. S2*, complements the cellular uptake for different incubation concentrations and for different stem cells donors.

**Chondrogenic, Adipogenic, and Osteogenic Differentiation of Magnetic Stem Cells.** MSCs harboring intracellular nanoparticles were further differentiated along the three most common differentiation pathways—chondrogenesis, adipogenesis, and osteogenesis—or kept undifferentiated. For each pathway, 4 h after nanoparticles incorporation, MSCs are either aggregated into small spheroids of 200,000 cells (3D model, mostly for chondrogenesis), or deposited in wells (again 200,000 cells) and stimulated with the appropriate differentiation factors. Because the cells almost reached confluence from day 1, and because they start rapidly to differentiate, they stopped dividing along the time course of the differentiation process, as shown in *SI Appendix, Fig. S3* for the adipogenic condition. Upon 21 d of differentiation, cells labeled with nanoparticles all expressed the genes specific to their differentiation pathway similarly to unlabeled cells, except for chondrogenesis at high dose where the differentiation level was down-regulated, yet not inhibited (Fig. 1 *G–K*). Representative histological images of each differentiation are shown in Fig. 1 *L–N*, for the low intracellular dose of iron per cell. Chondrogenic differentiation (Fig. 1*L*) was assessed with Safranin O, which reflects the presence of the glycosaminoglycan chains composing proteoglycans (stained in red). Adipogenic induction (Fig. 1*M*), analyzed with oil red O, was apparent by the accumulation of lipid-rich vacuoles (stained in red). Osteogenic differentiation (Fig. 1*N*) analyzed with alizarin red S showed calcium mineralization (stained in red).

**Magnetism as a Fingerprint of the Nanoparticles Intracellular Status: From Degradation to Neosynthesis.** Magnetic analyses were then performed over time to assess nanoparticles' degradation level depending on the differentiation status (Fig. 2). If one just compares the magnetic curves obtained at day 21 (Fig. 2 *A–D*), the difference between differentiation pathways is striking. First, for chondrogenesis, the cells lose more than 60% of their initial magnetization (Fig. 2*A*). *SI Appendix, Fig. S4* documents this important intracellular degradation as a function of the initial

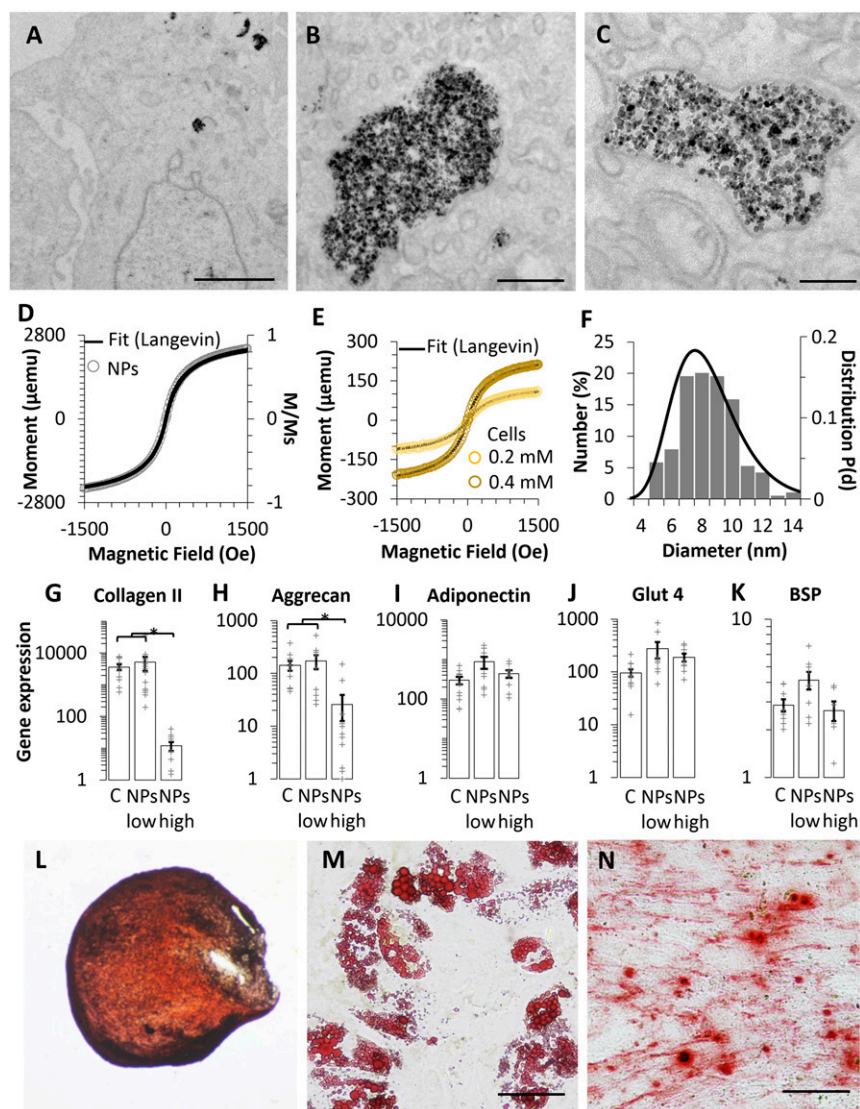


**Fig. 1.** Stem cell differentiation model for the study of magnetic nanoparticles intracellular transformations. (A–C) Transmission electron microscopy (TEM) of cell inner structure at day 0 shows endosomes filled with nanoparticles upon a 30-min incubation time at [Fe] = 0.2 mM. [Scale bar: 2 μm (A), 200 nm (B), and 100 nm (C).] (D) Magnetometry measurement of the initial solution of nanoparticles (10 μL at [Fe] = 8 mM). The Langevin's fit (plain line) is superposed on the data and corresponds to sizes distribution parameters  $d_{mag} = 8.4$  nm and  $\sigma = 0.31$ . (E) Magnetometry measurement of 200,000 cells right after incubation (day 0) with the nanoparticles at a concentration of [Fe] = 0.2 or 0.4 mM. For each curve, the Langevin's fit is superposed, corresponding to sizes distribution parameters of ( $d_{mag} = 8$  nm;  $\sigma = 0.26$ ) and ( $d_{mag} = 8.3$  nm;  $\sigma = 0.3$ ), respectively. (F) Diameter of the particles observed by TEM in the cells at day 0 (histogram bars and primary axis). Diameters were measured with ImageJ. The log-normal distribution of magnetic diameters deduced from the Langevin fit (parameters  $d_{mag}$  and  $\sigma$ ) is superposed (plain curve and secondary axis). (G–K) Expression of genes specific of each differentiation pathway at day 21 for unlabeled cells [control (C)], cells labeled with a low dose of nanoparticles ( $\leq 10$  pg/cell), and cells labeled with a high dose of nanoparticles ( $> 30$  pg/cell). Expression was normalized to RPLP0 mRNA and expressed relative to the average negative control value (undifferentiated MSCs) at day 21. Collagen II (G) and Aggrecan (H) are typically expressed under chondrogenesis and are impacted by a high dose of nanoparticles. Adiponectin (I) and glucose transporter type 4 (Glut4) (J) are typically expressed under adipogenesis and are not impacted by nanoparticle labeling. Bone sialoprotein (BSP) (K) is typically expressed under osteogenesis and is not impacted by nanoparticle labeling. (L–N) Histology images of cells labeled with a low dose of nanoparticles and differentiated in chondrocytes, adipocytes, and osteocytes for 21 d. (L) Section of a chondrogenesis spheroid stained with safranin O showing the presence of glycosaminoglycans. (M) Adipocytes stained with oil red O displaying the presence of lipid droplets. (N) Osteocytes analyzed with alizarin red S showing calcium mineralization. (Scale bar: 100 μm.)

nanoparticles' dose, and relatively to the three different donors. In the three other cases (adipogenesis, osteogenesis, and undifferentiated MSC in Fig. 2 B–D), 21 d after nanoparticles incorporation, the cells present the same (or almost) magnetization. That the nanoparticles were not degraded would be the immediate conclusion. However, the magnetic measurements at intermediate times (days 1, 3, and 9, Fig. 2 F–H) evidence that the nanoparticles were first degraded quite massively (up to 57% loss of the cellular magnetism), until day 3. Then, in between day 3 and day 9, the stem cells magnetism (re)increases, not only in a significant way ( $P < 0.01$  between day 3 and day 9) but also extremely unexpectedly in terms of amount of magnetization gained. For instance, for the adipogenic condition, where the (re)magnetization process is the most impressive, the cell sample gains 68 μemu (see *SI Appendix, Fig. S5* for typical magnetism curves). Per cell, such a magnetic increase corresponds to the appearance of about five million of magnetic nanoparticles of 8.4-nm size. Importantly, the analysis of total iron content (by elemental analysis, integrating both intact magnetic nanoparticles, and nonmagnetic iron from nanoparticles degradation products) showed that it did not vary from day 0 to day 21, whatever the condition (*SI Appendix, Fig. S6*). Any explanation involving an expulsion of iron is thus excluded. This surprising

pattern can only be explained through the reformation of magnetic iron *in cellulo* upon degradation of internalized iron oxide nanoparticles. Importantly, similar patterns were systematically observed, either for the same donor with independent experiments including different doses (*SI Appendix, Fig. S7A*), as well as between donors (*SI Appendix, Fig. S7B*).

Fig. 3 documents further the remagnetization phenomenon, under the adipogenic condition. It includes more time measurements (days 0, 1, 2, 3, 5, 9, and 14), and it shows three orthogonal methods of iron determination. First, magnetometry measurements (always on 200,000 cells) presented in Fig. 3A confirm the pattern observed in Fig. 2F. Second, the mass of iron in the same samples [measured by inductively coupled plasma (ICP) elemental analysis] is shown in Fig. 3B and accounts for all iron species present in the sample, magnetic and nonmagnetic. It shows that total iron does not vary over the different days, confirming the results of *SI Appendix, Fig. S6*, and evidencing that no iron leakage occurs. Other analytical chemical methods such as spectrophotometric assays (45) would also lead to the measurement of total iron content in the cellular sample, but not iron within a nanoparticle superparamagnetic structure, which can only be assessed by magnetic measures. Finally, we performed additional magnetic measurements using a third method that allows quantification at

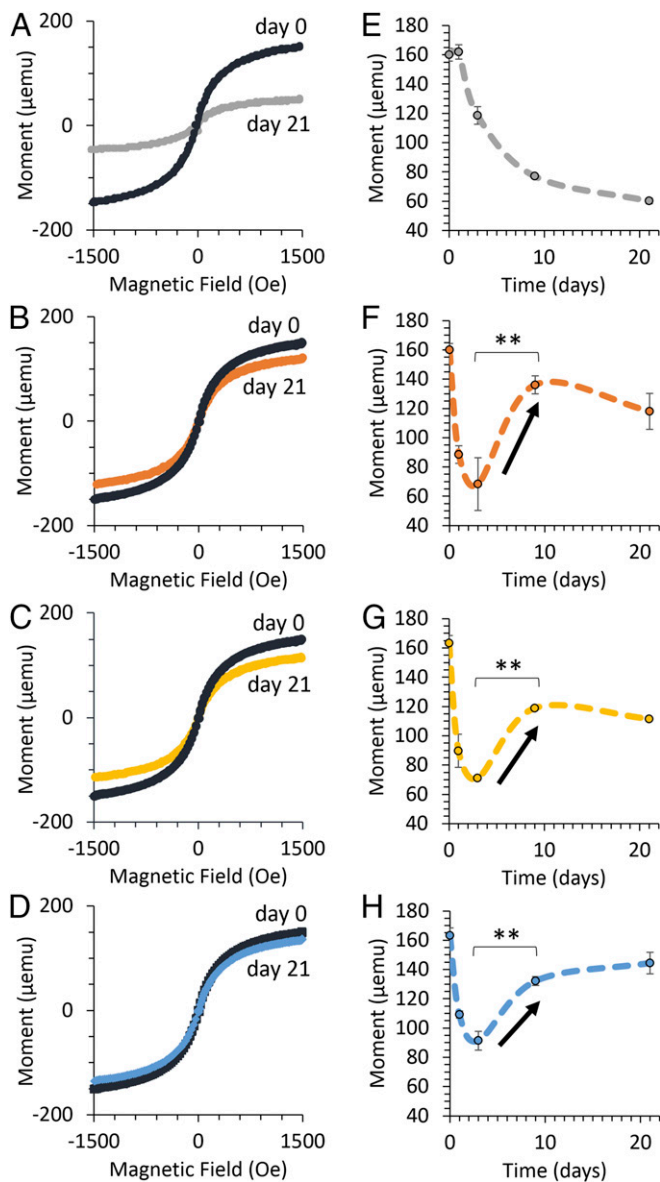


**Fig. 2.** Magnetometry to follow nanoparticles' transformations: Evidence of a remagnetization phenomenon. (A–D) VSM: Typical magnetization curves obtained for each pathway at day 0 and 21. (E–H) Average mass of magnetic iron per sample during maturation. Under chondrogenesis (A and E), the magnetic mass progressively decreased from day 0 to 21. For adipogenesis (B and F), osteogenesis (C and G), and the undifferentiated MSCs (D and H), a significant decrease of the magnetic mass is observed at days 1 and 3, compared with day 0. The magnetic mass then increases from day 3 to day 9 (indicated by black arrows) and remains constant at day 21. The results are the average of three independent experiments of three samples each. The error bars represent the SEM.

the single-cell level (Fig. 3C). It consists in a magnetophoretic analysis of the motion of single cells toward a permanent magnet creating a uniform magnetic field gradient  $\text{grad}B$  (35, 46). Each cell, with a magnetic moment  $m_{\text{cell}}$ , is submitted to a magnetic force  $m_{\text{cell}} \times \text{grad}B$  and migrates in return at constant velocity  $v_{\text{cell}}$  imposed by the balancing of the magnetic force with the Stokes viscous force ( $3\pi\eta R_{\text{cell}}v_{\text{cell}}$ , with  $\eta$  being the water viscosity and  $R_{\text{cell}}$  being the cell radius). Typical cell motions are illustrated in Fig. 3D at different days upon nanoparticles internalization. Motions of 100 single cells were analyzed for each condition and the average  $m_{\text{cell}}$  is shown in Fig. 3C. *SI Appendix, Fig. S8* also

shows the distribution of the magnetic moments over the cell population. Remarkably, the same pattern is observed at this single-cell level, confirming the remagnetization, with a decrease of the cell magnetic moment during the first days, followed by a significant increase.

**Imaging Nanoparticles' Transformations.** TEM imaging was then conducted to explore the structural status of the nanoparticles at day 21. For the chondrogenic condition, where the nanoparticles were found to be more than 60% degraded, TEM images revealed two types of nano-objects (Fig. 4A). The first one resembles the initial nanoparticles observed at day 0 (Fig. 1A–C), with a highly visible dark contrast and located in the endosomes only. The second type, less dense and smaller in size, is observed in both the endosomes and the cytoplasm. The two types of nano-objects present halos typical of iron oxides in overfocused TEM images (*SI Appendix, Fig. S9A and B*); however, electron diffraction analysis focused on the less dense and smaller nano-objects do not show any distinctive rings (Fig. 4B and *SI Appendix, Fig. S12A*). It indicates a poorly crystalline structure, consistent with ferrihydrite. The size distribution of all nano-objects is represented on the histogram of Fig. 4C. In average, their diameter is smaller ( $6.8 \pm 0.14$  nm) than at day 0 ( $8.5$  nm,  $P < 0.01$ ), with a clear difference between the ones located in endosomes ( $7.5 \pm 0.28$  nm, mix of the two types of nano-objects) and within the cytoplasm ( $6.1 \pm 0.07$  nm, second type of nano-objects only) ( $P < 0.01$ ) (*SI Appendix, Fig. S10*). These endosomal and cytoplasmic 6-nm nano-objects perfectly correspond to the size of the iron storage protein ferritin loaded with iron under the ferrihydrite form (47–50), iron coming from the nanoparticles' degradation as previously demonstrated (39). The magnetic diameter obtained by Langevin analysis is represented by the plain line of Fig. 4C. It reflects only magnetic nanoparticles and was found to be  $8.5 \pm 0.14$  nm with polydispersity 0.27, similar to the one calculated at day 0. As a result, size measurements extracted from TEM and from magnetism do not overlap anymore (Fig. 4C).

For the adipogenic condition, experiencing the remagnetization process, the picture is remarkably different. First, iron oxides are observed only in the endosomes, where they are gathered in clumps (Fig. 4D; see also *SI Appendix, Figs. S9C and S11* for the demonstration on unfocused images and for other views, respectively). Electron diffraction analysis focused on these iron oxides display distinctive rings (Fig. 4E and *SI Appendix, Fig. S12B*) characteristic of the inverse spinel structure of magnetite or maghemite (*SI Appendix, Fig. S13*). Their average size distribution, obtained from TEM images measurements, is  $8.2$  nm with a polydispersity of 0.27 (see histogram of Fig. 4F). The magnetic diameter obtained by Langevin analysis is also found at  $8.4$  nm with polydispersity of 0.29 (see plain line of Fig. 4F). Both distributions are superposed in Fig. 4F, with excellent overlapping, demonstrating that the nano-materials observed by TEM are all magnetic, to the contrary of previous observations made for the chondrogenic condition. One can finally notice that the magnetic diameter at day 21 is similar to the one at day 0, demonstrating that the reformed nanoparticles have a size around 8 nm in diameter, with important polydispersity. This is very logical, as the initial nanoparticles were produced by a most natural chemical synthesis based on iron salts coprecipitation. Finally, we should also emphasize that the presence of iron oxides in the endosomes suggests that the intracellular neosynthesis of nanoparticles happens in situ in the endosomes, where the iron degradation products of the initial nanoparticles are first released.

The intracellular localization of iron at day 21 was further confirmed by Prussian blue staining (Fig. 5). In the chondrocytes, blue dots are observed in addition to a diffuse blue color throughout the cytoplasm (Fig. 5A), indicating that iron is present

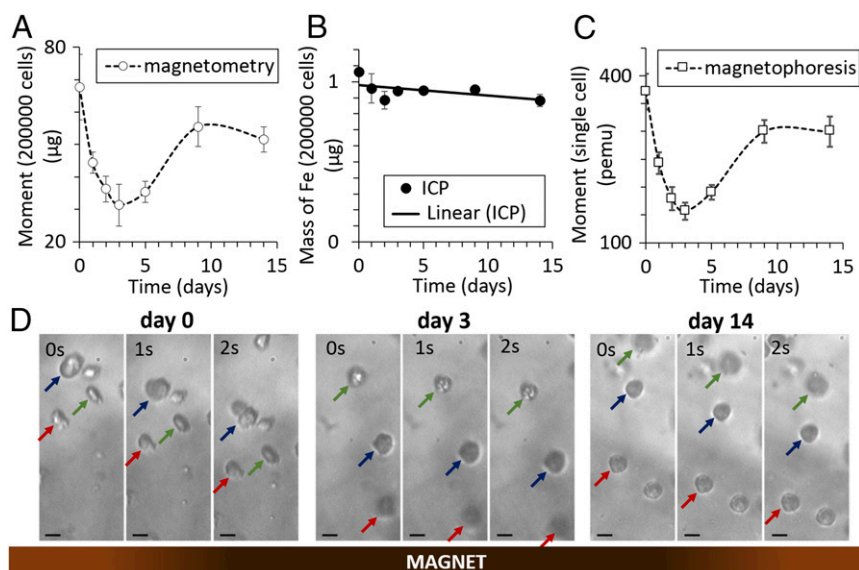


**Fig. 3.** Orthogonal magnetic and iron measurements during the remagnetization process. (A) Magnetometry measurement for the adipogenic condition (donor 3), starting with 200,000 cells, and measuring the total magnetization (expressed in micro-electromagnetic units, that is,  $10^{-6}$  emu) of the cell sample at different days (days 0, 1, 2, 3, 5, 9, and 14;  $n = 3$  for each condition). (B) ICP measurement of the total iron present in each cellular sample (same samples of 200,000 cells each), including both magnetic and nonmagnetic forms. (C) Magnetophoresis measurement at the single-cell level. For each condition, 100 cells were tracked, their velocity computed, and their magnetic moment  $m_{\text{cell}}$  calculated (expressed here in pico-electromagnetic units, that is  $10^{-12}$  emu). The average of three independent samples is shown at each day. (D) Typical images of cell migration (1-s interval between each image) at day 0, day 3, and day 14, showing that the cells first migrate more slowly from day 0 to day 3, and then recover almost the same speed at day 14. More specifically, the speed of each specific cell indicated by an arrow are  $(34, 42, 33) \mu\text{m}\cdot\text{s}^{-1}$ ,  $(12, 11, 14) \mu\text{m}\cdot\text{s}^{-1}$ , and  $(28, 30, 26) \mu\text{m}\cdot\text{s}^{-1}$ , for the day 0, 3, and 14 conditions, respectively. The specific magnetic moment calculated (proportional to both the cell speed and radius) are  $(419, 344, 348)$  pemu,  $(121, 142, 164)$  pemu, and  $(386, 327, 296)$  pemu, for days 0, 3, and 14, respectively.

both within endosomes and throughout the cytoplasm. In the adipocytes, only blue dots are observed at lysosomal localization (Fig. 5B). Immunostaining of ferritin reveals similar patterns with both dots and a diffuse staining in the chondrocytes (Fig. 5C), but only dots in the adipocytes reflecting lysosomal localization (Fig. 5D).

**Impact of Degradation and Neosynthesis on Iron Metabolism.** Gene expression of proteins involved in iron metabolism (described in scheme of Fig. 6A) are the main targets to give insight in the processes of nano-degradation versus nano-neosynthesis of magnetic iron oxides. Five genes were monitored: L-Ferritin (light chain of ferritin involved in iron binding and nucleation), H-Ferritin (heavy chain of ferritin, with ferroxidase activity), Ferroportin (iron export), divalent metal transporter DMT1 [transport of Fe(II) across cell membranes], and transferrin receptor TfR1 (iron import).

First of all, cells handle iron in a different manner depending on the differentiation pathway even without nanoparticles (Fig. 6B–D). For chondrogenesis, a down-regulation of transferrin is observed (SI Appendix, Fig. S14) as well as a major up-regulation of ferroportin, significantly higher than for the other pathways ( $P < 0.01$ ) (Fig. 6B). This decreased expression of iron import transferrin and increased expression of iron export ferroportin may indicate that, when undergoing chondrogenesis, a lower amount of iron is necessary.

The presence of magnetic nanoparticles additionally impacted the expression of some genes, such as ferroportin that increased for all pathways (Fig. 6B). Very interestingly, an overexpression of L-Ferritin is observed under chondrogenesis, while an overexpression of H-Ferritin is detected for all of the other pathways (Fig. 6C and D). This result provides two different storage approaches: in chondrogenesis, the L-ferritin is involved in typical iron storage (nonmagnetic ferrihydrite in the ferritin core), while in the other pathways the H-Ferritin (high ferroxidase activity) is

involved in the remagnetization process. DMT1 was almost unchanged by nanoparticle exposure (SI Appendix, Fig. S14). Transferrin was slightly down-regulated for labeled cells of all pathways at day 1 and day 21. Overall, these results indicate that, for all pathways, magnetic nanoparticles slightly inhibit iron internalization (transferrin down-regulated) and induce both iron export (ferroportin up-regulated) and storage (ferritin up-regulated). Storage strategies vary between cells experiencing intracellular nanodegradation (L-Ferritin overexpression) and cells presenting remagnetization (H-Ferritin overexpression).

To further demonstrate that nanoparticles intracellular synthesis is mediated by ferritin, we mimicked the conditions inside the endosomes after undergoing nanoparticles degradation generating molecular iron precursors, and in presence or absence of ferritin or apoferritin (SI Appendix, Fig. S15). This *ex cellulo* model confirmed that the remagnetization was higher when ferritin and apoferritin proteins are on site.

Expression of genes previously described as potential human homologs to the magnetotactic bacteria genes that are involved in the synthesis of magnetosomes was also assessed (SI Appendix, Tables S2 and S3) (51–53). Results displayed in SI Appendix, Fig. S16 indicate few significant differences between the cells labeled or not with nanoparticles. Under adipogenesis, pathway for which the remagnetization is observed, only PEX5 is overexpressed (potential homolog of mamA).

**A Role of Environmental Factors in Nanoparticles in Cellulo Neosynthesis?** Various environmental factors were next checked to probe their potential impact on the remagnetization process: proliferation status, 2D versus 3D cell culture, hypoxia, and additives [insulin–transferrin–selenium (ITS) Premix] acting on the iron metabolism pathway.

Reducing the proliferation level of undifferentiated MSCs (low serum condition) partly inhibited the remagnetization process (Fig. 7A). An initial decrease in magnetism from day 0 to

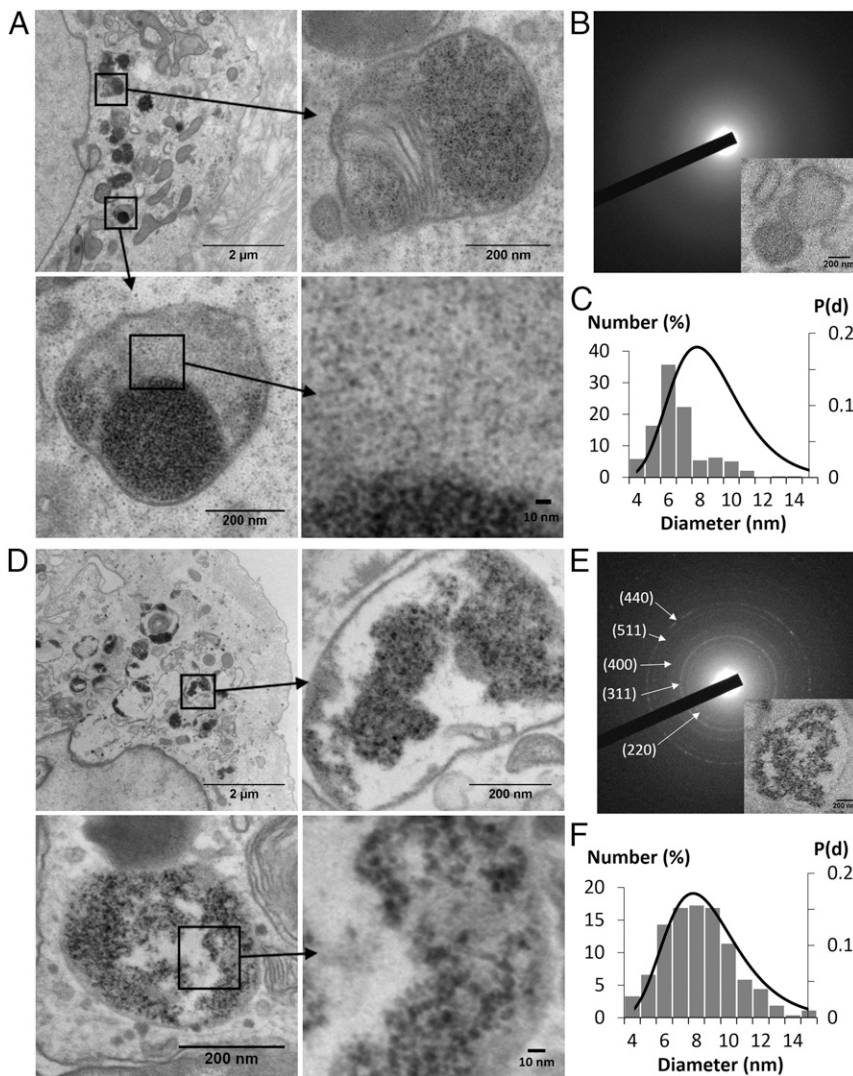


**Fig. 4.** Nanoparticle imaging within the tissue: Evidence of nanoscale transformations. (A and D) TEM bright-field images of cells containing nanoparticles after 21 d of maturation in chondrogenesis (A) or adipogenesis (D) conditions. (A) Under chondrogenesis, at day 21, remaining nanoparticles are present in the endosomes; however, most of them contain lighter color nanospots identified as ferritin. In the *Top Right* image, only ferritin is present in the endosome. In the *Bottom Left* image, the endosome is a hybrid, filled with both ferritin and intact nanoparticles. Ferritin spots are also detected outside the endosomes, throughout the cytoplasm (see *SI Appendix, Fig. S10* for additional images). (D) Under adipogenesis, at day 21, the endosomes are filled with both ferritin and nanoparticles that form a lump. Neither ferritin spots nor nanoparticles are detected outside the endosomes (see *SI Appendix, Fig. S11* for additional images). (B and E) Selected area electron diffraction patterns of typical endosomes at day 21 (targeted endosomes are shown in the boxed images). (B) Under chondrogenesis, no diffraction rings are observed, which coincides with iron stored as ferrihydrite in the endosomal ferritin. (E) Under adipogenesis, diffraction rings are observed that can be indexed to common lattice planes in the magnetite or maghemite crystal structure. (C and F) Diameter of the nanoparticles observed in TEM was measured with ImageJ (histogram bars and primary axis) and magnetic diameter log-normal distribution was obtained by fitting the magnetization curves with Langevin formalism (pondered by log-normal distribution) (curves and secondary axis). (C) Under chondrogenesis, the average magnetic diameter is different from the size of the particles observed in TEM, while (F) under adipogenesis, magnetic nanoparticles and all nanoparticles observed in TEM have a similar diameter.

1 was still observed, but then the cellular magnetic moments reached a plateau, signature of either a stop in the degradation process, or the occurrence of neosynthesis events at earlier time, yet less efficient than in normal conditions (see the lower final magnetization value at day 21).

Cell organization in 2D versus 3D had a significant impact (Fig. 7B), where the 3D (aggregate) structure inhibited the remagnetization process, with magnetism values reaching a plateau from day 3 to day 21. Intriguingly, values were similar at day 0 and 1, further confirming that 3D cellular organization in a spheroid inhibits the immediate degradation observed in all other 2D cases (from day 0 to day 1: systematic decrease).

As oxygen is known to interact with iron metabolism processes (54), the effect of hypoxia on the remagnetization was assessed (Fig. 7C). The only difference observed in low oxygen condition was a less marked initial degradation (day 3). However, the remagnetization process still occurred, with a significant magnetic increase from day 3 to day 9.

By contrast, adding 1% ITS Premix (one of the supplemental factors for the chondrogenesis differentiation) to cells in adipogenic conditions (experiencing the most pronounced remagnetization phenomenon) totally inhibited the remagnetization (Fig. 7D). The magnetic measurements then resembled the decrease always observed for chondrogenesis (except for a higher initial decrease imputed to the 2D culture). The 1% ITS

Premix enriches the medium with insulin, transferrin, selenious acid, and linoleic acid. As the insulin component was already present in the typical adipogenesis composition, it demonstrates that transferrin, selenious acid, linoleic acid, or their combination, stops the neo-synthesis.

### Discussion

The presence of biogenic magnetic nanoparticles has been identified in a variety of living organisms, including magnetotactic bacteria, insects, mollusks, birds, honey bees, and fish (1, 55). Upon initial detection of magnetic nanoparticles in humans brain samples in 1992 (56), magnetic materials have also been located in various human tissues, including heart, spleen, liver, ethmoid bone, and tumors (57–60). However, questions still remain regarding their role that may have a status from normal to abnormal depending on the species. In bacteria, for example, magnetite is determined as involved in detection of the geomagnetic field, which facilitates orientation and navigation (61). In humans, their presence is controversial as they have been associated with diseased tissues, with a higher prevalence in the brain cells of Alzheimer's patients (62). As iron oxide nanoparticles are present in both healthy and diseased tissues in humans, the possible key factor between normal and abnormal might be the dose of nanoparticles.



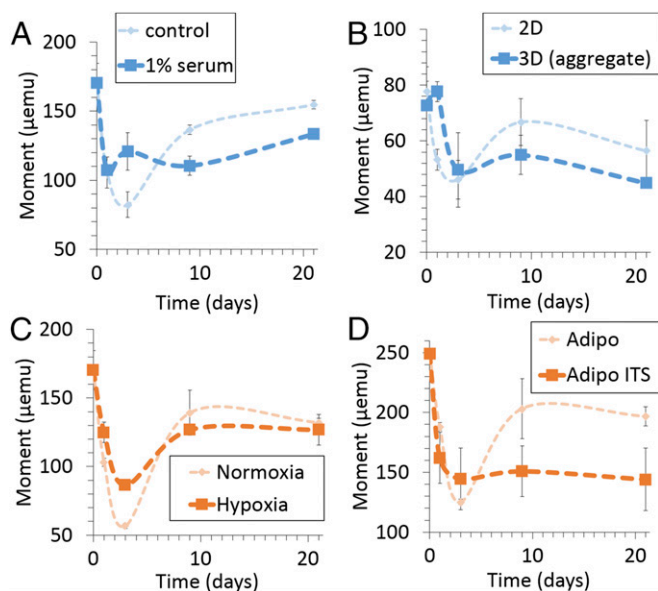


**Fig. 7.** Impact of culture parameters on nanoparticles' transformations. Magnetometry measurements were used to assess the effects of various culture parameters on the remagnetization. (A) Effect of proliferation studied on undifferentiated MSCs. Regular culture conditions (10% FBS) were compared with a low-serum (1% FBS) environment where cells remained alive but stopped dividing. This low proliferation inhibited the remagnetization. (B) Effect of a 3D culture in aggregate was compared with a 2D environment on undifferentiated MSCs. The 3D culture stopped the remagnetization. Interestingly, no degradation was observed between day 0 and day 1 similarly to the chondrogenic culture. (C) Effect on hypoxia (3% O<sub>2</sub>) studied under adipogenesis and compared with normoxia. Hypoxia had a limited effect on the remagnetization that was reduced, but however not inhibited. (D) Effect of ITS Premix (insulin–transferrin–selenium, a component of the chondrogenic medium), added to the adipogenic differentiation medium in the same concentration as the chondrogenic media (1%), was assessed. The addition of 1% ITS Premix to the culture medium inhibited the remagnetization. The error bars represent SEM.

Also very worth mentioning, H-ferritin was described to act as an antiinflammatory and antiapoptotic gene (70, 71), suggesting that it can be linked to a detoxification mechanism. This seems particularly relevant considering that MSCs exposed to high doses of magnetic nanoparticles present alterations of their differentiation potential under chondrogenesis, while none under adipogenesis and osteogenesis at similar concentrations. Remarkably, nanoparticles are simply degraded under chondrogenesis, while cells were remagnetized under the two other conditions. Storage under the magnetic form encouraged by the H-subunit of ferritin thus probably decreases the amount of reactive iron species in the cells and avoids toxicity even at high nanoparticles doses. By contrast, under a more classical degradation process, nanoparticles degradation products are progressively stored predominantly via the L-subunit of ferritin (as ferrihydrite). The classical storage approach under ferrihydrite in the ferritin might be less efficient at reducing reactive oxygen species levels leading to toxicity while under chondrogenesis.

Finally, we also evidence that remagnetization is a delicate process easily influenced by cellular factors. The fact that remagnetization does not happen under chondrogenesis might also be explained by the specific culture conditions required for the differentiation. Indeed, cells are subjected to reduced proliferation rate, culture in aggregate, and ITS supplementation (insulin–transferrin–selenium, components linked to iron metabolism), three parameters that independently inhibited the remagnetization and might act in synergy under chondrogenesis. Interestingly, only the 3D conformation (aggregate) retained the

similar magnetism level between day 0 and day 1 typically observed under chondrogenesis. The important initial degradation observed under the other conditions seems primordial as, without it, the remagnetization is inhibited. It suggests that the massive initial release of soluble iron might trigger the remagnetization. However, it is not the unique requirement, since even with an important initial degradation, under low proliferation and ITS-Premix supplementation, the process does not happen. It would actually be interesting to determine whether neosynthesis is stem cell specific or can be expanded to other cells, such as macrophages, which are known to play a primary role in nanoparticles intake when administered to an organism.

To conclude, these data evidence the possible synthesis of magnetic nanoparticles *in cellulo* linked to an excess of iron delivered by nanoparticles degradation, and involving the ferritin protein. Such magnetic nanoparticle neosynthesis is associated with an excellent tolerance of stem cells toward high doses of nanoparticles exposure. By contrast, in condition where it does not occur, the stem cells differentiation is impacted by important doses of nanoparticles. It thus suggests that the *de novo* synthesis is linked to a detoxification process attempted by the cells in the case of an iron excess. A recent review focused on magneto-reception draws similar conclusions: It demonstrates that the magnetite structures observed in migratory birds that have long been suspected to be involved in magnetoreception might actually just be a way for organisms to deposit excess iron (72).

## Methods

**Citrate-Coated Iron Oxide Nanoparticles.** Iron oxide (maghemite) nanoparticles were synthesized via the Massart procedure. Briefly, the ionic precursor was produced by alkaline coprecipitation of ferrous and ferric chlorides. The magnetite (Fe<sub>3</sub>O<sub>4</sub>) obtained was then chemically oxidized into maghemite (γ-Fe<sub>2</sub>O<sub>3</sub>) and dispersed in water. They were then stabilized via citrate chelation that complexes with the nanoparticles' ferric oxide surface and confers negative surface charges due to the carboxylate groups (COO<sup>-</sup>). The negatively charged surface is sufficient to ensure nanoparticles stability in aqueous suspension by electrostatic repulsion. The magnetic nanoparticles obtained exhibit a typical superparamagnetic behavior with mass magnetization of 65 emu/g of iron and present a log-normal size distribution with mean value of 8.4 nm and polydispersity of 0.35. Each 8.4-nm nanoparticle bears a magnetic moment of 6.8 × 10<sup>-17</sup> emu and weights in average of 10<sup>-18</sup> g of iron.

**Cell Culture and Nanoparticle Labeling.** Human MSCs (Lonza) from three different donors (aged from 21 to 23) were cultured in MSC growth medium (MSCGM) (Lonza) at 37 °C with 5% CO<sub>2</sub>. All cells were tested positive at more than 90% for the specific markers CD105, CD166, CD44, CD90, and CD73; and negative at less than 10% for the markers CD14, CD34, CD45, HLA-DR, and CD19. Cells were grown until passages 4–5 and at 80% confluence before labeling. All of these cell features may be of importance for the nanobio interface behavior (73). A labeling solution was prepared with nanoparticles diluted at [Fe] = 0.05–0.8 mM in serum-free RPMI culture medium (Thermo Fisher Scientific) supplemented with 5 mM free citrate (to avoid nanoparticles' precipitation). Incubation lasted for 30 min at 37 °C. Cells were then rinsed thoroughly in serum-free RPMI medium and incubated for 4 h with complete MSCGM medium before further processing.

**Cell Differentiation: Chondrogenesis, Osteogenesis, and Adipogenesis.** Labeled and unlabeled MSCs were subjected to adipogenic, osteogenic, and chondrogenic differentiation. For adipogenesis, 200,000 cells were plated per well of six-well plates (well area, 9.5 cm<sup>2</sup>). Two independent media were prepared: Adipogenic Induction Medium (AIM) and Adipogenic Differentiation Medium (ADM). AIM consisted of high-glucose DMEM (Thermo Fisher Scientific) supplemented with 10% FBS, 1% penicillin–streptomycin (Thermo Fisher Scientific), 10 ng/mL insulin (Sigma), 1 μM dexamethasone (Sigma), 200 μM indomethacin (Sigma), and 500 μM isobutyl methylxanthine (Sigma). ADM was made of high-glucose DMEM supplemented with 10% FBS, 1% penicillin–streptomycin, and 10 ng/mL insulin. Adipogenesis was induced in AIM for 3–4 d followed by ADM for 3 d. The treatment was repeated three times, and then cells were maintained in ADM until day 21 with media replenished twice a week. Cells maintained in MSCGM medium replenished twice a week served as negative control. At day 21, cells were fixed in 10% formalin (Sigma) and subjected to oil red O staining (Sigma) to detect

cytoplasmic triglyceride. For osteogenesis, 200,000 cells per well were seeded in six-well plates and grown for 2 d in MSCGM medium for cell attachment and proliferation up to confluence. Osteogenesis was then induced in low-glucose DMEM (Thermo Fisher Scientific) supplemented with 10% FBS, 1% penicillin–streptomycin, 0.1 μM dexamethasone, and 50 μM L-ascorbic acid 2-phosphate (Sigma), and 10 mM β-glycerophosphate (Sigma). The medium was replenished twice a week and cells maintained in MSCGM served as negative control. Calcium mineralization was determined using alizarin red staining. After 21 d of differentiation, cells were fixed in 10% formalin, washed with deionized water, and stained 5 min at room temperature with 2% alizarin red S (Sigma), rinsed with tap water, and then counterstained with 1% light green (Sigma). For chondrogenesis, 200,000 cells were centrifuged (260 × g for 5 min) to form a high-density pellet. Pellets were then cultured in serum-free high-glucose DMEM supplemented with 1% penicillin–streptomycin, 0.1 μM dexamethasone, 1 mM sodium pyruvate, 50 μM L-ascorbic acid 2-phosphate, 0.35 mM L-proline (Sigma), 1% ITS Premix (Corning), and 10 ng/mL TGF-β3 (Interchim). Pellets cultured in the same medium without TGF-β3 served as negative controls. The medium was replenished twice a week. After 21 d of differentiation, pellets were fixed in 10% formalin, frozen in OCT compound (VWR), sectioned (8-μm-thick slices), and stained with Safranin O (0.1%) (Sigma) for 3 min at room temperature to detect glycosaminoglycans.

**Iron Quantification.** Total iron dosage was performed by ICP atomic emission spectrometer (model iCAP6200 duo; Thermo Fisher Scientific). For each measurement, cell samples were digested in 200 μL of boiling 70% nitric acid (trace metal basic grade; Sigma) for 1 h at 100 °C. The solutions were then diluted in filtered ultrapure water for analysis. Calibration standards and quality controls were provided by SCP SCIENCE and ChemLab. Analyzer drift is corrected by regular quality controls measurements to ensure a drift inferior to 5%. Autosampler ASX-520 was used. Argon 4.5 Linde (min, 99.995%) was used as plasma and purge gas. Samples were analyzed in 2% HNO<sub>3</sub>.

**Prussian Blue Imaging.** Prussian blue staining was performed to locate iron in the cells. Samples fixed in 10% formalin were stained with Prussian blue [5% potassium ferrocyanide (Sigma) in 10% hydrochloric acid (Sigma-Aldrich)] for 35 min and counterstained with nuclear fast red (Sigma) for 15 min.

**Immunofluorescence of Ferritin.** Samples were fixed with 4% paraformaldehyde (Interchim) for 10 min at room temperature. After washing with PBS, cells were permeabilized with PBS–Triton X-100 [0.2% (vol/vol)] for 10 min. Nonspecific sites were blocked with 5% (wt/vol) BSA diluted in PBS–Triton X-100 [0.1% (vol/vol)] during 2 h and incubated overnight at 4 °C with anti-ferritin primary antibody (EPR3004Y; Abcam) diluted 1:100 in 1% BSA PBS–Triton X-100 [0.1% (vol/vol)]. After several PBS washings, the Alexa Fluor 488-conjugated anti-rabbit IgG secondary antibody (A32731; Thermo Fisher) diluted 1:500 in 1% BSA PBS was incubated for 3 h at room temperature. Cells were washed with PBS, and their nuclei were stained with DAPI diluted 1:1,000 in PBS for 20 min at room temperature and mounted with a drop of Fluoromount (Sigma-Aldrich). Cells were analyzed with an Olympus JX81/BX61 device/Yokogawa CSU device spinning-disk microscope (Andor Technology), equipped with a 63× oil objective (Olympus).

**Samples Magnetometry and Log-Normal Size Distribution Analysis of the Nanoparticles.** Magnetism values of fixed samples were analyzed at days 0, 1, 3, 9, and 21 using a vibrating sample magnetometer (VSM) (Quantum Design; Versalab). Field-dependent magnetization curves were measured at 300 K as a function of the external field. A low range of –150 to +150 mT (step rate of 10 mT/s) was first performed to obtain precise measurements. A higher range of 0–3,000 mT (step rate of 30 mT/s) then provided magnetization at saturation. The magnetic moment M recorded (in electromagnetic units) could be converted into grams of magnetic iron m<sub>Fe</sub> (65 emu/g of iron) as each material reached magnetization at saturation.

The percentage of degradation between day 0 and day 21 is then simply calculated as follows:  $(1 - (m_{Fe}(\text{day 21})/m_{Fe}(\text{day 0})))$ .

Langevin analysis can also be performed on the magnetization curve to determine the size distribution of the nanoparticles in situ. First, the size of the nanoparticles population is generally described as a log-normal distribution:  $P(d) = (1/(\sqrt{2\pi\sigma^2})) \times \exp(-(\ln^2(d/d_{mag}))/2\sigma^2)$ .  $\sigma$  is the polydispersity index, and  $d_{mag}$  is the characteristic magnetic diameter, namely the two parameters describing the nanoparticles size. The magnetic moment of the nanoparticles sample can then be written as the Langevin law  $M(H) = m_s\phi(\coth \xi - 1/\xi)$ , weighted by  $P(d)$ .  $\xi = 10^{-4}M_s\pi d^3 B/6kT$  is the Langevin parameter,  $B$  being the applied magnetic field;  $k$ , the Boltzmann constant;  $T$ , the temperature; and  $M_s$ , the saturation magnetization of the magnetic material.

**RNA Isolation, cDNA Synthesis, and Quantitative RT-PCR.** Total RNA was isolated using NucleoSpin RNA kit (Machery-Nagel) according to the manufacturer's instructions. To avoid genomic DNA contamination, RNA samples were incubated for 15 min with 10 U of DNase. cDNA was then synthesized using SuperScript II Reverse Transcriptase kit (Thermo Fisher Scientific) with random hexamers according to the manufacturer's instructions. Real-time PCR analysis was then carried out with SYBR Green PCR technology using the StepOnePlus system (Thermo Fisher Scientific). The expression of 60S acidic ribosomal protein P0 (*RPLP0*) was used as a reference transcript. The sequences of primers used are presented in *SI Appendix, Table S1*.

**TEM.** Nanoparticle-labeled cells were harvested 3 h upon labeling (day 0) and at day 21 for chondrogenesis and adipogenesis. Harvested cells were rinsed and fixed with 5% glutaraldehyde in 0.1 mol/L sodium cacodylate buffer (Sigma-Aldrich), and postfixed with 1% osmium tetroxide solution (Sigma) containing 1.5% potassium cyanoferrate (Sigma). Cells were then gradually dehydrated in ascending concentrations of ethanol and embedded in Epon resin. Thin sections (70 nm) were examined with a FEI-Tecnaï 12 transmission electron microscope at 80 kV (ImagoSeine, Institut Jacques Monod, Paris, France). Size analysis of the structures made of crystalline iron (recognized by their halo when the image is unfocused) was performed using ImageJ. TEM bright-field images and selected area electron diffraction patterns were recorded on a Jeol 2100F equipped with a Schottky emission gun and a Gatan US 4000 CCD camera.

**Ex Cellulo Model.** Nanoparticles were degraded in a solution of citrate excess (nanoparticles, 20 mM; citrate, 40 mM) at pH 4 and 37 °C. Degradation level of the nanoparticles was monitored via VSM, and solutions were used when no trace of nanoparticle was detected. The degradation product of the nanoparticles resulted in an excess of Fe(III) as determined using potassium thiocyanate (KSCN in HCl) (Sigma) to detect Fe(III) and ferrozine (Sigma) to detect Fe (II). The pH was then adjusted to 5, and the degradation product was mixed with either water, apoferritin (Sigma), or ferritin (Sigma). Solutions were placed at 37 °C under 5% CO<sub>2</sub> for 21 d, and then VSM measurements were performed.

**Statistical Analysis.** All values are presented as mean ± SEM. Significance between two groups was determined using independent Student's *t* test, and significance between three or more groups was determined using one-way ANOVA. If ANOVA indicated significance at  $P < 0.05$ , a Tukey (honestly significant difference) post hoc test was performed to compare group means. For all values, a minimum of 95% confidence level was considered significant, with  $*P < 0.05$  and  $**P < 0.01$ . Number of independent measurements was systematically superior to 3 ( $n > 3$ ).

**ACKNOWLEDGMENTS.** We thank Aude Michel for synthesis of nanoparticles and Ana Espinosa for fruitful discussion. We are also grateful to Christine Péchoux from Mima2 platform-Inra (Jouy en Josas) for TEM analysis. We acknowledge the CNanoMat platform (University Paris 13) for access to the magnetometry facility. We thank Laure Cordier for ICP measurements, at the Institut de Physique du Globe de Paris (IPGP) platform, supported by IPGP multidisciplinary program PARI (Plateau d'analyse haute résolution), and by Paris-IdF Region SESAME (Soutien aux équipes scientifiques pour l'acquisition de moyens expérimentaux) Grant 12015908. This work was supported by the European Union (ERC-2014-CoG Project MaTissE 648779).

- Baumgartner J, et al. (2013) Magnetotactic bacteria form magnetite from a phosphate-rich ferric hydroxide via nanometric ferric (oxyhydr)oxide intermediates. *Proc Natl Acad Sci USA* 110:14883–14888.
- Amor M, et al. (2015) Chemical signature of magnetotactic bacteria. *Proc Natl Acad Sci USA* 112:1699–1703.
- Gieré R (2016) Magnetite in the human body: Biogenic vs. anthropogenic. *Proc Natl Acad Sci USA* 113:11986–11987.
- Wang YX, Hussain SM, Krestin GP (2001) Superparamagnetic iron oxide contrast agents: Physicochemical characteristics and applications in MR imaging. *Eur Radiol* 11:2319–2331.
- Schwenk MH (2010) Ferumoxytol: A new intravenous iron preparation for the treatment of iron deficiency anemia in patients with chronic kidney disease. *Pharmacotherapy* 30:70–79.
- Chertok B, et al. (2008) Iron oxide nanoparticles as a drug delivery vehicle for MRI monitored magnetic targeting of brain tumors. *Biomaterials* 29:487–496.
- Bull E, et al. (2014) Stem cell tracking using iron oxide nanoparticles. *Int J Nanomedicine* 9:1641–1653.
- Wu W, Wu Z, Yu T, Jiang C, Kim W-S (2015) Recent progress on magnetic iron oxide nanoparticles: Synthesis, surface functional strategies and biomedical applications. *Sci Technol Adv Mater* 16:023501.

9. Revia RA, Zhang M (2016) Magnetite nanoparticles for cancer diagnosis, treatment, and treatment monitoring: Recent advances. *Mater Today (Kidlington)* 19:157–168.
10. Thanh NT (2018) *Clinical Applications of Magnetic Nanoparticles: From Fabrication to Clinical Applications* (CRC Press, Boca Raton, FL).
11. Wei H, et al. (2017) Exceedingly small iron oxide nanoparticles as positive MRI contrast agents. *Proc Natl Acad Sci USA* 114:2325–2330.
12. Espinosa A, et al. (2018) Magnetic (hyper)thermia or photothermia? Progressive comparison of iron oxide and gold nanoparticles heating in water, in cells, and in vivo. *Adv Funct Mater* 28:1803660.
13. Lu C-W, Hsiao J-K, Liu H-M, Wu C-H (2017) Characterization of an iron oxide nanoparticle labelling and MRI-based protocol for inducing human mesenchymal stem cells into neural-like cells. *Sci Rep* 7:3587.
14. Du V, et al. (2017) A 3D magnetic tissue stretcher for remote mechanical control of embryonic stem cell differentiation. *Nat Commun* 8:400.
15. Zheng B, et al. (2016) Quantitative magnetic particle imaging monitors the transplantation, biodistribution, and clearance of stem cells in vivo. *Theranostics* 6: 291–301.
16. Landázuri N, et al. (2013) Magnetic targeting of human mesenchymal stem cells with internalized superparamagnetic iron oxide nanoparticles. *Small* 9:4017–4026.
17. Weissleder R, et al. (1989) Superparamagnetic iron oxide: Pharmacokinetics and toxicity. *AJR Am J Roentgenol* 152:167–173.
18. Bourrinet P, et al. (2006) Preclinical safety and pharmacokinetic profile of ferumoxtran-10, an ultrasmall superparamagnetic iron oxide magnetic resonance contrast agent. *Invest Radiol* 41:313–324.
19. Ruiz A, et al. (2013) Biodistribution and pharmacokinetics of uniform magnetite nanoparticles chemically modified with polyethylene glycol. *Nanoscale* 5:11400–11408.
20. Mejias R, et al. (2013) Long term biotransformation and toxicity of dimercaptosuccinic acid-coated magnetic nanoparticles support their use in biomedical applications. *J Control Release* 171:225–233.
21. Kolosnjaj-Tabi J, et al. (2016) Biotransformations of magnetic nanoparticles in the body. *Nano Today* 11:280–284.
22. Kreyling WG, et al. (2015) *In vivo* integrity of polymer-coated gold nanoparticles. *Nat Nanotechnol* 10:619–623.
23. Lartigue L, et al. (2013) Biodegradation of iron oxide nanocubes: High-resolution in situ monitoring. *ACS Nano* 7:3939–3952.
24. Ruiz A, et al. (2015) Biotransformation of magnetic nanoparticles as a function of coating in a rat model. *Nanoscale* 7:16321–16329.
25. Laskar A, Ghosh M, Khattak SI, Li W, Yuan X-M (2012) Degradation of superparamagnetic iron oxide nanoparticle-induced ferritin by lysosomal cathepsins and related immune response. *Nanomedicine (Lond)* 7:705–717.
26. Lévy M, et al. (2010) Degradability of superparamagnetic nanoparticles in a model of intracellular environment: Follow-up of magnetic, structural and chemical properties. *Nanotechnology* 21:395103.
27. Silva AH, et al. (2016) Superparamagnetic iron-oxide nanoparticles mPEG350- and mPEG2000-coated: Cell uptake and biocompatibility evaluation. *Nanomedicine (Lond)* 12:909–919.
28. Lee C-M, et al. (2013) Nonpolymeric surface-coated iron oxide nanoparticles for in vivo molecular imaging: Biodegradation, biocompatibility, and multiplatform. *J Nucl Med* 54:1974–1980.
29. Heidari F, Bahrololoom ME, Vashae D, Tayebi L (2015) In situ preparation of iron oxide nanoparticles in natural hydroxyapatite/chitosan matrix for bone tissue engineering application. *Ceram Int* 41:3094–3100.
30. Luciani N, et al. (2016) Successful chondrogenesis within scaffolds, using magnetic stem cell confinement and bioreactor maturation. *Acta Biomater* 37:101–110.
31. El Haj AJ, et al. (2015) An in vitro model of mesenchymal stem cell targeting using magnetic particle labelling. *J Tissue Eng Regen Med* 9:724–733.
32. Souza GR, et al. (2010) Three-dimensional tissue culture based on magnetic cell levitation. *Nat Nanotechnol* 5:291–296.
33. Fayol D, et al. (2013) Use of magnetic forces to promote stem cell aggregation during differentiation, and cartilage tissue modeling. *Adv Mater* 25:2611–2616.
34. Yamamoto Y, et al. (2011) Functional evaluation of artificial skeletal muscle tissue constructs fabricated by a magnetic force-based tissue engineering technique. *Tissue Eng Part A* 17:107–114.
35. Fayol D, Luciani N, Lartigue L, Gazeau F, Wilhelm C (2013) Managing magnetic nanoparticle aggregation and cellular uptake: A precondition for efficient stem-cell differentiation and MRI tracking. *Adv Healthc Mater* 2:313–325.
36. Chang Y-K, Liu Y-P, Ho JH, Hsu S-C, Lee OK (2012) Amine-surface-modified superparamagnetic iron oxide nanoparticles interfere with differentiation of human mesenchymal stem cells. *J Orthop Res* 30:1499–1506.
37. Kostura L, Kraitchman DL, Mackay AM, Pittenger MF, Bulte JWM (2004) Feridex labeling of mesenchymal stem cells inhibits chondrogenesis but not adipogenesis or osteogenesis. *NMR Biomed* 17:513–517.
38. Henstock JR, Rotherham M, Rashidi H, Shakesheff KM, El Haj AJ (2014) Remotely activated mechanotransduction via magnetic nanoparticles promotes mineralization synergistically with bone morphogenetic protein 2: Applications for injectable cell therapy. *Stem Cells Transl Med* 3:1363–1374.
39. Mazuel F, et al. (2016) Massive intracellular biodegradation of iron oxide nanoparticles evidenced magnetically at single-endosome and tissue levels. *ACS Nano* 10: 7627–7638.
40. Fortes Brolo ME, et al. (2018) Magnetic properties of nanoparticles as a function of their spatial distribution on liposomes and cells. *Phys Chem Chem Phys* 20:17829–17838.
41. Mourdikoudis S, Pallares RM, Thanh NTK (2018) Characterization techniques for nanoparticles: Comparison and complementarity upon studying nanoparticle properties. *Nanoscale* 10:12871–12934.
42. Mazuel F, et al. (2017) Magneto-thermal metrics can mirror the long-term intracellular fate of magneto-plasmonic nanohybrids and reveal the remarkable shielding effect of gold. *Adv Funct Mater* 27:1605997.
43. Soukup D, Moise S, Céspedes E, Dobson J, Telling ND (2015) In situ measurement of magnetization relaxation of internalized nanoparticles in live cells. *ACS Nano* 9:231–240.
44. Amiri H, et al. (2013) Protein corona affects the relaxivity and MRI contrast efficiency of magnetic nanoparticles. *Nanoscale* 5:8656–8665.
45. Hedayati M, et al. (2018) An optimised spectrophotometric assay for convenient and accurate quantification of intracellular iron from iron oxide nanoparticles. *Int J Hyperthermia* 34:373–381.
46. Plan Sangnier A, et al. (2018) Targeted thermal therapy with genetically engineered magnetite magnetosomes@RGD: Photothermia is far more efficient than magnetic hyperthermia. *J Control Release* 279:271–281.
47. Pan Y, et al. (2006) Electron beam damage studies of synthetic 6-line ferrihydrite and ferritin molecule cores within a human liver biopsy. *Micron* 37:403–411.
48. Pan Y-H, et al. (2009) 3D morphology of the human hepatic ferritin mineral core: New evidence for a subunit structure revealed by single particle analysis of HAADF-STEM images. *J Struct Biol* 166:22–31.
49. Gálvez N, et al. (2008) Comparative structural and chemical studies of ferritin cores with gradual removal of their iron contents. *J Am Chem Soc* 130:8062–8068.
50. Jian N, Dowe M, Horniblow RD, Tselepis C, Palmer RE (2016) Morphology of the ferritin iron core by aberration corrected scanning transmission electron microscopy. *Nanotechnology* 27:46LT02.
51. Gorobets O, Gorobets S, Koralewski M (2017) Physiological origin of biogenic magnetic nanoparticles in health and disease: From bacteria to humans. *Int J Nanomedicine* 12: 4371–4395.
52. Gorobets O, Gorobets S, Gorobets Y (2014) *Biogenic Magnetic Nanoparticles: Biomineralization in Prokaryotes and Eukaryotes* (Taylor and Francis, New York), pp 300–308.
53. Medvediev O, Gorobets OY, Gorobets SV, Yadrkhinsk'y VS (2017) The prediction of biogenic magnetic nanoparticles biomineralization in human tissues and organs. *J Phys Conf Ser* 903:012002.
54. Chepelev NL, Willmore WG (2011) Regulation of iron pathways in response to hypoxia. *Free Radic Biol Med* 50:645–666.
55. Shaw J, et al. (2015) Magnetic particle-mediated magnetoreception. *J R Soc Interface* 12:0499.
56. Kirschvink JL, Kobayashi-Kirschvink A, Woodford BJ (1992) Magnetite biomineralization in the human brain. *Proc Natl Acad Sci USA* 89:7683–7687.
57. Brem F, et al. (2006) Magnetic iron compounds in the human brain: A comparison of tumour and hippocampal tissue. *J R Soc Interface* 3:833–841.
58. Kobayashi A, Yamamoto N, Kirschvink J (1997) Studies of inorganic crystals in biological tissue: Magnetite in human tumor. *J Jpn Soc Powder Powder Metall* 44: 294–300.
59. Sant'Ovaia H, Marques G, Santos A, Gomes C, Rocha A (2015) Magnetic susceptibility and isothermal remanent magnetization in human tissues: A study case. *Biomaterials* 28: 951–958.
60. Baker RR, Mather JG, Kennaugh JH (1983) Magnetic bones in human sinuses. *Nature* 301:79–80.
61. Yan L, et al. (2012) Magnetotactic bacteria, magnetosomes and their application. *Microbiol Res* 167:507–519.
62. Pankhurst Q, Hautot D, Khan N, Dobson J (2008) Increased levels of magnetic iron compounds in Alzheimer's disease. *J Alzheimers Dis* 13:49–52.
63. Maher BA, et al. (2016) Magnetite pollution nanoparticles in the human brain. *Proc Natl Acad Sci USA* 113:10797–10801.
64. Liu X, Theil EC (2005) Ferritins: Dynamic management of biological iron and oxygen chemistry. *Acc Chem Res* 38:167–175.
65. Fitak RR, Wheeler BR, Ernst DA, Lohmann KJ, Johnsen S (2017) Candidate genes mediating magnetoreception in rainbow trout (*Oncorhynchus mykiss*). *Biol Lett* 13: 20170142.
66. Quintana C, Cowley JM, Marhic C (2004) Electron nanodiffraction and high-resolution electron microscopy studies of the structure and composition of physiological and pathological ferritin. *J Struct Biol* 147:166–178.
67. Martínez-Pérez MJ, et al. (2010) Size-dependent properties of magnetoferritin. *Nanotechnology* 21:465707.
68. Melnikova L, et al. (2015) SANS contrast variation study of magnetoferritin structure at various iron loading. *J Magn Magn Mater* 377:77–80.
69. Liße D, et al. (2017) Engineered ferritin for magnetogenetic manipulation of proteins and organelles inside living cells. *Adv Mater* 29:1700189.
70. Berberat PO, et al. (2003) Heavy chain ferritin acts as an antiapoptotic gene that protects livers from ischemia reperfusion injury. *FASEB J* 17:1724–1726.
71. Pham CG, et al. (2004) Ferritin heavy chain upregulation by NF- $\kappa$ B inhibits TNF $\alpha$ -induced apoptosis by suppressing reactive oxygen species. *Cell* 119:529–542.
72. Mouritsen H (2018) Long-distance navigation and magnetoreception in migratory animals. *Nature* 558:50–59.
73. Mahmoudi M (2018) Debugging nano-bio interfaces: Systematic strategies to accelerate clinical translation of nanotechnologies. *Trends Biotechnol* 36:755–769.